Manipulator Design and Operation of a Six-Degree-of-Freedom Handheld Tremor-Canceling Microsurgical Instrument

Sungwook Yang, *Student Member, IEEE*, Robert A. MacLachlan, *Member, IEEE*, and Cameron N. Riviere, *Senior Member, IEEE*

Abstract—**This paper presents the design and actuation of a six-degree-of-freedom (6-DOF) manipulator for a handheld instrument, known as "Micron," which performs active tremor compensation during microsurgery. The design incorporates a Gough-Stewart platform based on piezoelectric linear motors, with a specified minimum workspace of a cylinder 4 mm long and 4 mm in diameter at the end-effector. Given the stall force of the motors and the loading typically encountered in vitreoretinal microsurgery, the dimensions of the manipulator are optimized to tolerate a transverse load of 0.2 N on a remote center of motion near the midpoint of the tool shaft. The optimization yields a base diameter of 23 mm and a height of 37 mm. The fully handheld instrument includes a custom-built optical tracking system for control feedback, and an ergonomic housing to serve as a handle. The manipulation performance was investigated in both clamped and handheld conditions. In positioning experiments with varying side loads, the manipulator tolerates a side load up to 0.25 N while tracking a sinusoidal target trajectory with less than 20 μm error. Physiological hand tremor is reduced by about 90% in a pointing task, and error less than 25 μm is achieved in handheld circle-tracing.**

Index Terms—**Robot kinematics, motion compensation, surgery, medical robotics.**

I. INTRODUCTION

ROBOT-AIDED micromanipulation has been a focus of research in biomedical applications, since it offers a variety of advantages over conventional techniques [1]–[3]. For example, robotic platforms enable fine manipulation with high precision and dexterity during surgery by tremor filtering and also motion scaling [4], [5]. In addition, subtasks can be automated, alleviating the cognitive load of repetitive procedures and improving accuracy [6]. To provide a stable base for accurate manipulation, most platforms are mechanically grounded [7]–[9]. However, these systems involve potential risks during operation due to their relatively large range of motion and high inertia [10], the risk being exacerbated by the tendency of patients to move during surgery,

especially when merely sedated rather than anesthetized, as in ophthalmic surgery [11]. Teleoperation also involves a separation between surgeon and patient, and a lack of natural feel in manipulation.

To address the latter problems, a cooperative robot, the Steady Hand, has been developed, using shared control principles [12], [13]. The robot selectively complies with force/torque sensor input, allowing voluntary motion and suppressing tremor while a surgeon simultaneously holds the surgical instrument. The Steady Hand thus provides a more direct coupling to the human's natural kinesthetic sense [12]. However, the system still has the same drawback with respect to the possibility of patient movement [14].

As an alternative, a fully handheld micromanipulator, Micron, has been introduced, to retain the surgeon's direct manual control of gross positioning of the tool and to preserve the natural feel of manual operation [14], [15]. The handheld manipulator senses its own motion and selectively filters out erroneous motion such as hand tremor. The manipulator then produces stabilized motion at the tool tip via active error compensation. Despite its advantages in terms of usability, safety, and economy [15], the present system, 3-DOF Micron, still entails several drawbacks that must be overcome for practical use in microsurgery. First of all, due to the limited number of degrees of freedom (DOF) in manipulation, the system cannot offer a remote center of motion (RCM), as is generally required in most of minimally invasive surgery [16], [17]. In particular, for intraocular surgery, an RCM is necessary in order to avoid unwanted transverse movement at the point of entry through the sclera [17]. In addition, the range of motion at the tip of the current 3-DOF Micron system is limited to a few hundred micrometers due to the small displacement of the piezoelectric bender actuators used [15]. This results in frequent saturation of the actuators due to large or rapid motion of the hand. The limited range of motion also hinders Micron from being used in numerous applications such as patterned laser photocoagulation [18]. For such applications, an order-of-magnitude increase in the range of motion is needed [15]. Accordingly, a new 6-DOF handheld micromanipulator providing a larger range of motion has now been developed.

In order to realize the new manipulator, a parallel-link mechanism is preferable to a serial-link mechanism since it occupies a small volume and provides large angular

and resulting improvements in positioning performance. Specifically, the new optimization adds constraints to avoid collision with the instrument housing, and includes iteration in order to handle simultaneous optimization of coupled parameters; these were lacking in the previous work. Finally, the handheld performance of the manipulator is demonstrated.

II. Manipulator Design and Analysis

The goal is to make the instrument as narrow as possible, and in any case no wider than 25 mm. For the 6-DOF handheld micromanipulator, the Gough-Stewart platform [24], [25] is adopted, in order to take advantage of its high stiffness while still occupying small volume. In order to realize a miniature version of the parallel mechanism, several challenges should be addressed. First, the size constraint considerably limits the set of feasible actuators. Although a variety of miniature actuators has been introduced in realizing miniature mechanisms [26], [27] and some of them are commercially available, it is still challenging to obtain enough force or torque from them to provide reliable motion. For instance, micro DC motors may be adequate for the miniaturization of mechanisms in terms of size. However, they are commonly combined with high reduction gears to compensate for the low torque and also with a set of a thread and nut to convert rotational motion into linear motion, which leads to low speed as well as a complex and bulky mechanism.

For our application, we adopt the SQUIGGLE® motor (SQL-RV-1.8, New Scale Technologies, Inc., USA), a type of piezoelectric linear motor, since it is small enough (2.8 mm × 2.8 mm × 6 mm) and generates adequate force (>0.3 N at 3.3V). The motor utilizes the orbital vibration of the piezoelectric elements on it to generate linear motion of a threaded rod. Moreover, the linear stroke of the motor is adjustable to any value by selecting the length of the threaded rod, which provides us flexibility in the design and optimization of the manipulator.

A. Kinematics

The six degrees of freedom of the manipulator, considered in terms of the movements of interest for the microsurgical application, are as follows:

- Translation in XYZ Euclidean space at the tool tip (3-DOF);
- Translation in XY plane at a point somewhere along the tool shaft (2-DOF);
- Axial rotation of the tool (1-DOF).

The second translation tends to be constrained in robot-aided surgery to provide a fulcrum at the surgical incision point. For intraocular surgery, the desired workspace for the tool tip is a cylinder 4 mm in diameter and 4 mm long.

The inverse kinematics involves determination of the vector M_i corresponding to each link, given the position and orientation of the tool tip. The vector M_i is represented by the sum of vectors OA_i and OB_i in (1). Here, O and P are the
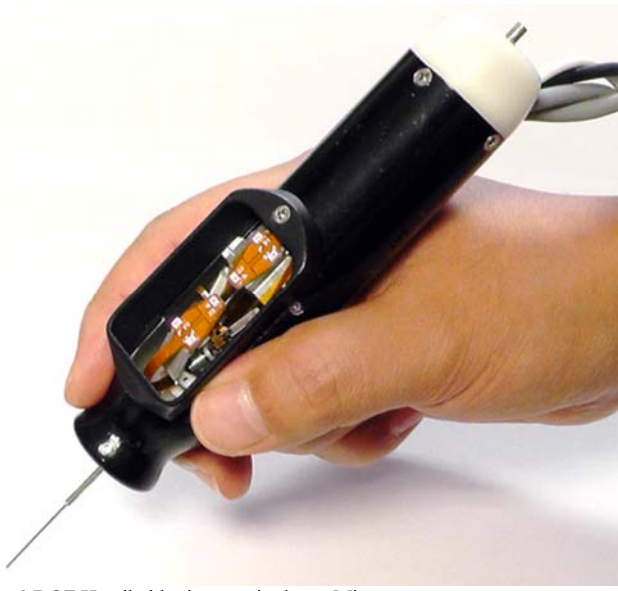

Fig. 1. 6-DOF Handheld micromanipulator, Micron.

displacement with high inherent stiffness [17]. Several 6-DOF parallel manipulators have already shown their potential in biomedical applications [10], [17], [19]–[21]. A 6-DOF parallel micromanipulator based on the Gough-Stewart platform was introduced for retinal surgery [17]. A dual structure of two 3-DOF parallel micromanipulators was also developed for cell micromanipulation [19]. In addition, Shoham *et al*. presented a smaller 6-DOF parallel micromanipulator using micromotors and embedded LVDT sensors [10]. However, these manipulators have to be mounted to a table or the skeleton of the patient due to their size. Manipulators presented in the literature that are of comparable size to Micron generally have only three degrees of freedom. Peirs *at el*. developed miniature parallel manipulators for steerable arms integrated in a self-propelled endoscope, based on hydraulic power. A motorized version of the manipulator was also developed, offering relatively large angular motion [20]. As for handheld operation, manipulators using piezoelectric actuators and flexure hinges for mechanical amplification have been introduced [21], [22]. Despite the mechanical amplification, the workspace of these handheld manipulators is limited to several hundred micrometers because of the small displacement of the piezoelectric stack actuators used—the factor which led to the development of the most recent 3-DOF Micron prototype [15], whose range of motion is larger, but still inadequate. In order to attain a much larger range of motion in a comparable size, an alternative actuation modality is necessary.

Therefore, we propose a new Micron design providing a larger range of motion and higher degrees of freedom in a smaller package using novel linear actuators. In preliminary reports of this research, a basic design based on a miniature Gough-Stewart platform was introduced and a benchtop version was built to evaluate the force capability and confirm the workspace of the manipulator [14], [23]. In this paper, we describe the development of a fully handheld micromanipulator, presented in Fig. 1, including refinements to the previously reported optimization and mechanical design,
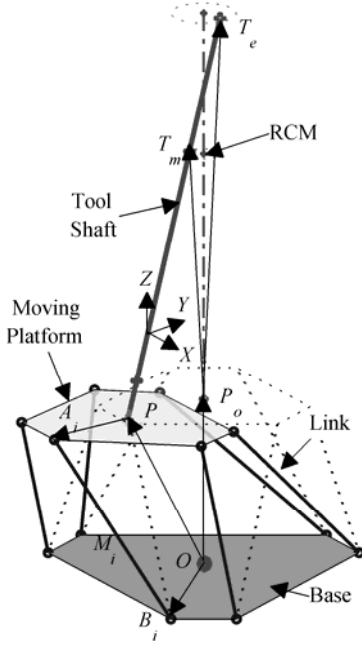
Fig. 2. Kinematic configuration of a 6-DOF parallel mechanism with a tool tip and a remote center of motion (RCM). The dotted lines represent the initial configuration and the solid lines a configuration with displaced tool tip and RCM.

origins of the base (fixed frame) and the moving platform, respectively, as shown in Fig. 2. A_i is one end of the ith link attached on the moving platform, which is defined with respect to the origin P. B_i is the other end of the ith link, at the base, defined with respect to the origin O.

$$M_i = OA_i - OB_i = OP + PA_i - OB_i \qquad (1)$$

In order to determine, OA_i the end and the middle positions of the tool tip P_0T_e and P_0T_m, respectively, are expressed by (2–3) with respect to the initial origin of the moving platform P_0.

$$P_0T_e = \begin{bmatrix} \Delta d_{ex} & \Delta d_{ey} & \Delta d_{ez} + l_t \end{bmatrix}^T \qquad (2)$$

$$P_0T_m = \begin{bmatrix} \Delta d_{mx} & \Delta d_{my} & d_{RCM} \end{bmatrix}^T \qquad (3)$$

The relative displacements from the initial positions of the tool tip are denoted by Δd_{ei} and Δd_{mi}, where the subscript i indicates each coordinate in the Euclidean space. The nominal length of the tool shaft is l_t. In addition, d_{RCM} is given by setting a remote center of motion with respect to the initial position of the moving platform. The unit vector of the tool tip u_t is then defined by two positions of the tool tip:

$$u_t = \frac{P_0T_e - P_0T_m}{|P_0T_e - P_0T_m|} = \begin{bmatrix} u_{tx} & u_{ty} & u_{tz} \end{bmatrix}^T \qquad (4)$$

The origin of the moving platform P is represented by the length of the tool and corresponding vectors OP_0, P_0T_e and u_t in (5).

$$OP = OP_0 + P_0T_e - l_t u_t \qquad (5)$$

The rotation of the moving platform is then expressed by the axis of rotation and the corresponding angle. The axis of the rotation $\hat{n}_{rot}$ is regarded as the cross product of the initial vector u_{init} (equivalent to the z-axis) and the current vector of the tool tip u_t in (6). The angle of the rotation is corresponding to the angle between two vectors u_{init} and u_t in (7).

$$\hat{n}_{rot} = \frac{u_{init} \times u_t}{|u_{init} \times u_t|} \qquad (6)$$

$$\theta_{rot} = \cos^{-1}(\mathbf{u}_{init}^T \mathbf{u}_t) \qquad (7)$$

, where u_{init} is $\begin{bmatrix} 0 & 0 & 1 \end{bmatrix}^T$.

Given the angle-axis rotation, a rotation matrix, $R_{ot}^{3\times3}$ is also defined using a matrix form of Rodrigues' rotation formula in (8) in order to construct a homogenous transform.

$$R_{ot}^{3\times3} = \cos\theta_{rot}I^{3x3} + \sin\theta_{rot}\hat{n}_{rot} \times I^{3x3} + (1-\cos\theta_{rot})\hat{n}_{rot}\hat{n}_{rot}^T \qquad (8)$$

, where I^{3x3} is an identity matrix of size 3.

The rotation matrix is also regarded as the combination of rotations with the Tait-Bryan (yaw-pitch-roll) angles α, β, and γ with respect to the initial position in (9).

$$R_{ot}^{3\times3} = X(\gamma)Y(\beta)Z(\alpha)$$
$$= \begin{bmatrix} C_\beta C_\alpha & -C_\beta C_\alpha & S_\beta \\ C_\gamma S_\alpha + C_\alpha S_\gamma S_\beta & C_\gamma C_\alpha - S_\gamma S_\beta S_\alpha & -C_\beta S_\gamma \\ S_\gamma S_\alpha - C_\gamma C_\alpha S_\beta & C_\gamma S_\alpha + C_\gamma S_\beta S_\alpha & C_\gamma C_\beta \end{bmatrix}, \quad \begin{array}{l} C_\theta \equiv \cos\theta \\ S_\theta \equiv \sin\theta \end{array} \qquad (9)$$

, where X, Y, and Z are the rotation matrices about each axis with an angle of θ.

In particular, the angles β and γ are simply derived by (10) using the components of the unit vector u_t with the axial rotation of the tool α assumed to be zero. This is because axial rotation does not change the tool tip position, and is therefore not needed in active tremor cancellation [14]. The corresponding angles are written in (11).

$$R_{ot}^{3\times3}u_{init} = u_t \qquad (10)$$

$$\beta = \sin^{-1}(u_{tx})$$
$$\gamma = -\tan^{-1}\left(\frac{u_{ty}}{u_{tz}}\right) \qquad (11)$$

Each end position OA_i of the ith link on the moving platform is determined by a homogeneous transform in (12), where the vector OP is regarded as translation of the moving platform.

$$\begin{bmatrix} OA_i^{3\times1} \\ 1 \end{bmatrix} = \begin{bmatrix} R_{ot}^{3\times3} & OP^{3\times1} \\ 0^{1\times3} & 1 \end{bmatrix} \begin{bmatrix} P_0A_i^{3\times1} \\ 1 \end{bmatrix} \tag{12}$$

The desired length of each link is finally determined by the vector of each link M_i using (1).

B. Generalized Force on Link

It is essential to analyze the generalized forces acting on the links in the design of the manipulator since the actuators used are relatively weak and prone to failure due to external force on the tool tip of the instrument. For the analysis, we introduce Plücker coordinates, which represent the vector of each link as six homogeneous coordinates. The representation offers convenient tools in analyzing the kinematics of the manipulator [28]. In addition to the force analysis, it is also useful for the singularity analysis of the manipulator, being combined with the screws and wrenches [29].

Let the unit screw $e_i^{1\times6}$ be the combination of two vectors q_i and q_{i0} in (13). Here, q_i represents the normalized vector of the ith link and q_{i0} is the cross product of PA_i and q_i.

$$e_i^{1\times6} = \begin{bmatrix} q_i & q_{i0} \end{bmatrix} = \begin{bmatrix} \dfrac{B_iA_i}{|B_iA_i|} & \dfrac{(PA_i \times B_iA_i)}{|B_iA_i|} \end{bmatrix} \tag{13}$$

Given each position of a link derived by the inverse kinematics, Plücker coordinates E are assigned by horizontally cascading each unit screw e_i in (14).

$$E^{6\times6} = \begin{bmatrix} e_1^T & e_2^T & e_3^T & e_4^T & e_5^T & e_6^T \end{bmatrix} \tag{14}$$

The velocity kinematics is completely described in (15) using the relationship between the generalized velocities of the links $\dot{\theta}$, the twist of the moving platform Ω, Plücker coordinates E and the matrix G.

$$E\Omega = G\dot{\theta} \tag{15}$$

, where $\dot{\theta}$ is composed by $\begin{bmatrix} \dot{\theta}_1 & \dot{\theta}_2 & \dot{\theta}_3 & \dot{\theta}_4 & \dot{\theta}_5 & \dot{\theta}_6 \end{bmatrix}^T$ and Ω is $\begin{bmatrix} V_x & V_y & V_z & \omega_x & \omega_y & \omega_z \end{bmatrix}^T$. In the Stewart platform, G is an identity matrix since each diagonal element is the scalar product of q_i and the vector of the generalized coordinate θ_i that also lies on each link. For any configuration with the full rank of the matrix E the generalized force F is derived as (16) upon an external wrench R.

$$F = G\begin{bmatrix} E^T \end{bmatrix}^{-1} R \tag{16}$$

, where R is $\begin{bmatrix} F_x & F_y & F_z & M_x & M_y & M_z \end{bmatrix}^T$. F is then represented as $\begin{bmatrix} f_1 & f_2 & f_3 & f_4 & f_5 & f_6 \end{bmatrix}^T$, where f_i is the signed magnitude of the force acting along each link.

C. Geometric Parameter Optimization

Our primary goal is to design the manipulator to be compact as possible for easy grip and also robust to external disturbance during operation, particularly transverse loading at the entry point through the sclera. This factor drives the optimization of geometric parameters such as diameters of the base and moving (or "top") platforms, and the length of the links.

Although various approaches have been introduced for optimization of the dimensions of parallel manipulators [30], [31], they primarily focus on the overall stiffness of the manipulators in order to withstand external loads and to achieve high control bandwidth. Hence, we need a new approach to consider the capabilities of actuators used in such a small manipulator. For instance, small actuators suitable for the compact package are weak in terms of force/torque. This may result in undesirable manipulation under the considerable force at the fulcrum because such actuators cannot overcome external force. Hence, to maintain the position of the tool tip even under heavy side load, the force distributed on each actuator by force and moment equilibrium should not exceed the maximum thrust force of the actuator. Otherwise, the actuator stalls and the manipulator cannot cancel hand tremor. Moreover, the design space is more limited in the case of the small manipulator since the actuators occupy most of the volume in the mechanical design of the manipulator.

The optimal dimension for the manipulator is therefore determined by the expected side load and the available thrust force. Specifically, the distributed force acts as either compression or tension to each link, depending on the direction of the side load. Considering transverse application of force to the tool tip in all possible directions, the external wrench R defined in (16), is rewritten in terms of a certain side load F_s and application angle θ_s in (17).

$$R = \begin{bmatrix} F_s\cos\theta_s & F_s\sin\theta_s & 0 & 0 & 0 & 0 \end{bmatrix}^T \tag{17}$$

We also define link force variation f_{var} using (16) upon the geometric parameters such as the diameters of the base and top and the nominal length of the links, denoted by D_b, D_t, and, L_m, respectively in (18).

$$f_{var}(D_b, D_t, L_m, F_s, \theta_s) = |\max(f_i) - \min(f_i)|, \quad i = 1\cdots6 \tag{18}$$

Given the side load and application angle, the force variation can be minimized by appropriate selection of the dimensions of the manipulator. Fig. 3 shows how the force variation (18) behaves given different geometric parameters when the transverse load is 0.2 N (determined from previous experiments
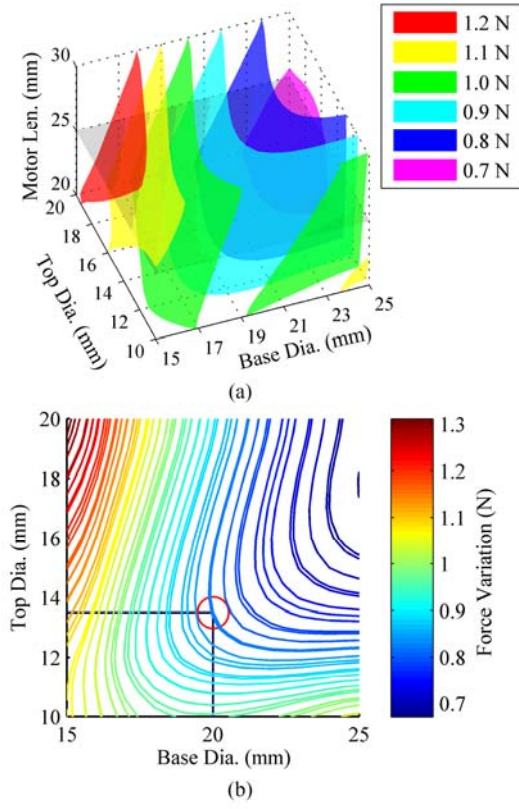
Fig. 3. (a) The force variation with respect to the varying geometric parameters of the manipulator for side load of 0.2 N acting at the RCM. (b). The contour of the force variation with respect to the base and the top diameters at a link length of 25 mm. The red circle indicates the optimal diameter of the moving platform when the upper bound of the base diameter is set at 20 mm.

[32]) and the angle of application varies from $-\pi$ to π around the RCM. For example, given a link length of 25 mm, larger base diameter and corresponding top diameter offer the minimum force variation, as shown in Fig. 3(b).

In order to find the optimal dimension for the manipulator, the cost function should minimize the force variation on the links at a nominal tool pose in (19), where the same amount of side load is applied with all angles of application used for simulating Fig. 3.

$$\arg\min_{D_b, D_t, L_m}(f_{var}(D_b, D_t, L_m, F_s, \theta_s)|_{F_s= 0.2\,N,\, \theta_s \in [-\pi,\pi]}) \quad (19)$$

Since the optimization tends to approach the upper limit of the base diameter, we set the largest feasible diameter of the base to 20 mm, taking into account the grip of the handheld manipulator. The parameters are optimized using a numerical approach based on the 'active-set' algorithm utilizing the Matlab^{TM} function 'fmincon.m,' which performs constrained nonlinear multivariable optimization. It can thus include not only upper and lower bounds of the parameters but also nonlinear inequality constraints. The additional constraints are important in the design for real-world use. For instance, moving components such as the links and the top must avoid collision with the housing. Moreover, the minimum allowable link length is a function of the other geometric parameters because it

is determined by the need to reach the predefined workspace.

The refined approach imposes two types of nonlinear inequality constraints on the optimization, driven by the predefined workspace. First, the largest displacement of the moving platform in the desired workspace is considered, to prevent the moving platform from going beyond the outer diameter of the base.

$$d_{Ur} < \frac{D_b}{2} \text{ and } d_{Lr} < \frac{D_b}{2}$$

, where d_{Ur} and d_{Lr} are the longest distances from the central axis of the manipulator to any edge of the moving platform at the upper and lower limit of the workspace, respectively. The second is to simultaneously update the lower bound of the link length while running the optimization, with respect to the nominal length and travel of the link. Since any parameter related to the workspace is not encoded in the cost function, the nominal length is regulated by this constraint in order to reach the entire workspace. Hence, we first introduce the minimal length of the link l_0, contributed by mechanical components such as a bearing assembly, which will be described later. The value is set to be 17.5 mm for the optimization. The longest and shortest lengths of the link are also defined by the linear mechanism as $l_0 + 2l_s$ and $l_0 + l_s$, where l_s is the total available travel of the link. Given any nominal length of the link during iteration, the maximum length of the link l_{max} required to reach the workspace must be less than or equal to the longest length, $l_0 + 2l_s$ and vice versa.

$$l_{max} \le l_0 + 2l_s \text{ and } l_{min} \ge l_0 + l_s$$

The optimization yields a top diameter of 13.3 mm and a link length of 25.1 mm at the upper bound of the base diameter, 20.0 mm, with force variation of 0.83 N. The amount of the force variation is acceptable with the range of the thrust force of the motor selected, ±0.5 N. The total travel of the linear motors is calculated to be 5.3 mm for covering the cylindrical workspace that we define.

D. Workspace Analysis

Given the optimization result, the reachable space of the manipulator is determined by applying pivoting motion about an RCM that is 35 mm above the moving platform. The space is fundamentally limited by the available travel of the link. Fig. 4 (a) depicts the reachable space in red for a travel of 5.3 mm derived from the optimization. The required cylindrical workspace shown as the blue in Fig. 4(a) is entirely covered by the reachable space.

Furthermore, we investigate the workspace with respect to the amount of side load that the manipulator can tolerate. In order to sustain the load, each motor should be able to support the axial load produced by the distribution of the side load. This is tantamount to regarding the stall force of the motor as the primary constraint in the optimization. Fig. 4(b) illustrates the

motion when no motion is introduced on the links.

A. Miniature 6-DOF Manipulator

We built a miniature 6-DOF manipulator based on piezoelectric linear motors as shown in Fig. 5, which allows maneuverability in the desired cylindrical workspace while withstanding side loads up to 0.25 N. The manipulator is composed of the top (Delrin), base (aluminum), and six legs incorporating the piezoelectric linear motors.

In order to use the linear motor in our platform, it is essential to incorporate a miniature bearing assembly that decouples the pure linear motion from screw motion combined with translation and rotation on the threaded rod. The assembly includes a miniature bearing (681h, Dynaroll Corp., USA; 1.0 mm thickness × 3.0 mm diameter), a motor coupler, a housing, and a retainer as shown in Fig. 6 (bottom).

Two mechanical stops limit the travel of the screw, in order to protect the manipulator from dismantling itself, and to avoid becoming locked by the threaded rod at the extremity of travel. One stop is located at the free end of the screw. This part is made of PTFE (Polytetrafluoroethylene), a soft and low-friction material, since the stopper is rotating as it contacts the motor body. The retainer doubles as an upper stop, preventing the motor coupler from being fastened onto the motor body like a screw head.

The upper and lower ends of the link are connected to the moving platform and the base by flexure hinges (#1-0 polypropylene suture). These feature smaller size and less friction than ball/universal joints [21], and are adequate given the small angular range of motion. Within the designated workspace, the maximum angular displacement of the flexure hinge is 10.9° and the corresponding stress is 20.8 MPa for a length of 2.5 mm, which is less than the yield stress of polypropylene (30.3 MPa).

A certain amount of preload on the SQUIGGLE® motors is required for proper operation, as it avoids backlash that would otherwise result from the loose fit between the threaded rod and
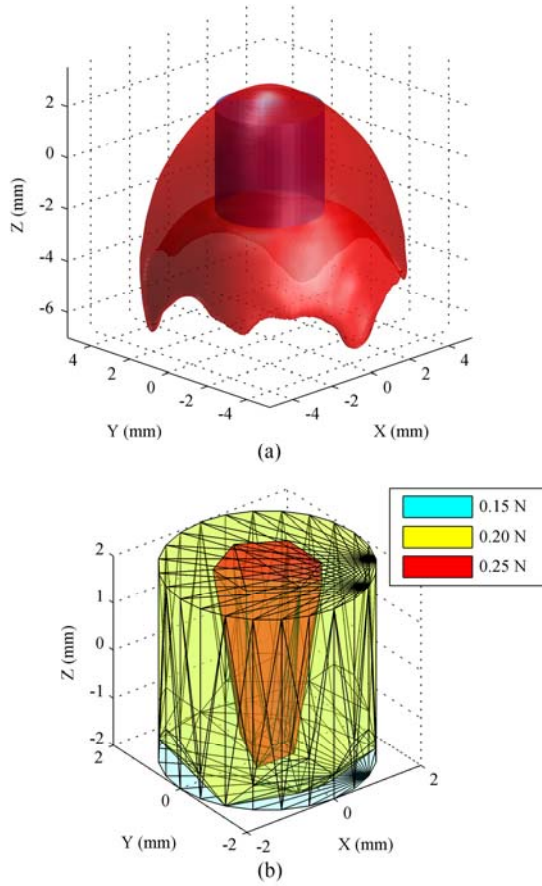

Fig.4. (a) Reachable space (red) obtained by pivoting the tool tip around a predefined RCM. The cylinder (blue) inside the space indicates the desired workspace. (b) The reachable space depending on applied side load.

available workspace with respect to the varying side loads from 0.15 to 0.25 N. The load can be tolerated up to 0.20 N in most of the cylindrical workspace, the exception being small regions near the workspace boundary, visible in Fig. 4(b). Although the higher load shrinks the available space, the design bears the load up to 0.25 N in the desirable workspace for canceling hand tremor. Beyond the load of 0.30 N, available workspace does not exist because the stall force of the actuator is assigned to be ±0.5 N.

In addition to the side load capability, desired workspace of the manipulator has also been analyzed for singularities, which may be encountered in such closed-loop kinematic chains [33]. Given the velocity kinematics (15), the manipulator undergoes a singularity if the determinant of either the matrix G or E is zero. However, the matrix G is uniquely defined as an identity matrix in our platform because the inverse kinematics provides a unique solution for the links in the relatively small workspace without rotation about the tool tip. Hence, non-zero instantaneous motion does not occur along active links when the moving platform is fully locked [29]. The matrix E also has full rank within the designated workspace, as it provides non-zero determinants during a grid search. This is led by setting the distance between the ends of adjacent links to be the smallest possible value; singularities can occur when the screw axes intersect or are parallel to each other [29]. As a result, the manipulator does not yield undesired and uncontrollable
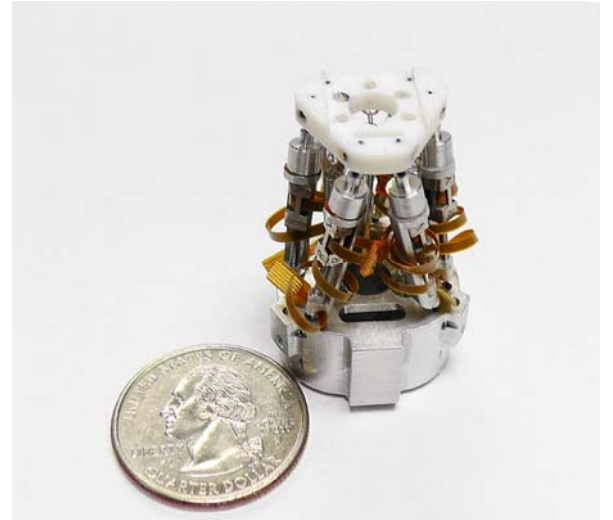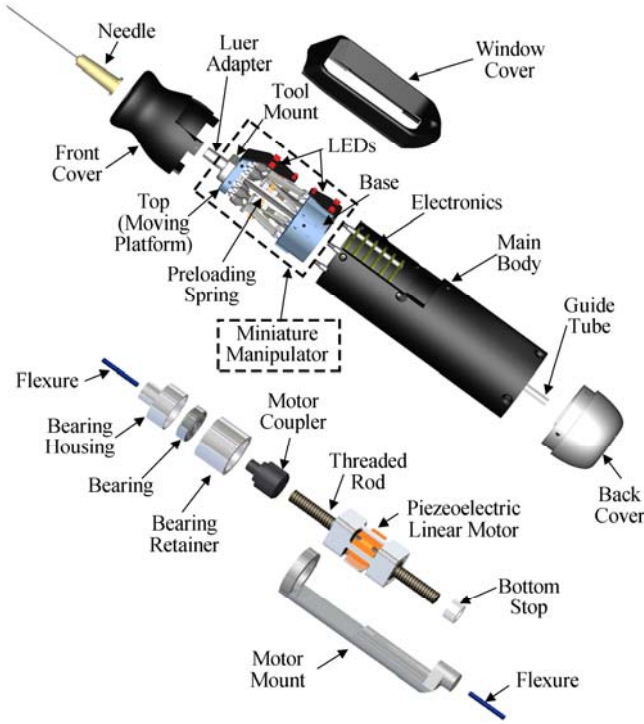

Fig. 5. Miniature 6-DOF manipulator, compared with a US quarter.

Fig. 6. Exploded view of the handheld manipulator assembly (top) and the linear actuation module (bottom).

TABLE I
SPECIFICATION OF 6-DOF MICRON

Description	Specification
Overall dimension[a]	Φ 28.5 × 126 mm
Total weight	70.0 g
Miniature manipulator	Φ 23.0 × 37.0 mm (14.4 g)
Workspace[b]	Φ 4.0 × 4.0 mm
Degrees of freedom	6
Side load capability[c]	up to 0.25 N
Actuator	Piezoelectric linear motor (SQUIGGLE® SQL-RV-1.8)
Position sensor	A custom-built optical tracking system (a sampling rate of 1 kHz over a 27 cm3 workspace, with less than 10 µm RMS noise)

[a]The dimension is for the entire housing, excluding the tool tip.
[b]The workspace is defined at the end of the tool tip with a fixed RCM.
[c]The maximum value is allowed at the center of the workspace; the manipulator can endure the sideload up to 0.15 N over the entire workspace.

the actuated "nut." To provide this preload, three tension springs are vertically aligned from the base to the moving platform. The minimum stiffness that avoids backlash is desirable in order to minimize variation of preload across the workspace, and to avoid using up the force capability of the motors just to overcome the preload. We opted for a spring with stiffness of 28.2 mN/mm (CI 010EF 14S316, Lee Spring, USA).

Each link weighs 0.3 g and the entire weight of all moving parts is only 2.3 g. It is consequently light enough to be free from degradation in dynamic performance due to excessive mass. The mechanism has an overall diameter of 23 mm and a height of 37 mm, with total weight of 14.4 g.

B. Handheld Manipulator Design

For the control of the manipulator, we adopted a custom-built microscale optical tracking system, "ASAP" (Apparatus to Sense Accuracy of Position) [34]. Compared to previous Micron prototypes incorporating inertial sensors [35]–[37], the optical tracking system is preferable in terms of size, accuracy, and speed. For good performance, we found that motion must be suppressed at frequencies below 1 Hz, which is lower than could be detected with the inertial sensing system in [35]. In addition, inertial sensing leads to drift in position measurement, which must be addressed with either sensor fusion or recalibration of sensors [36].

The manipulator is equipped with two sets of infrared LEDs, in order to enable optical tracking of the position and orientation of both the tool tip and the handle. Three LEDs are mounted to the moving platform and the other three are affixed to the handle (the LEDs are visible as small white blocks in Fig.

1). The position sensitive detectors (PSD) sense the differently modulated signals using frequency domain multiplexing and provide an analog position measurement of the centroid of each light source [34]. Consequently, the detectors allow each LED position to be triangulated in three dimensions and then the poses of the tool tip and handle are fully recovered from the position of each triad of LEDs [15]. The poses are acquired at a sampling rate of 1 kHz over a 27 cm3 workspace, with less than 10 µm RMS noise [34]. A PCB (printed circuit board) stack of six layers is attached to the bottom of the manipulator. The three layers of the PCB stack closest to the base of the manipulator drive the motors, which communicate with a main controller via inter-integrated circuit (I^2C) protocol. The remaining two layers are used for driving the LEDs for ASAP measurement. The last PCB routes the power and control signals to all upper PCBs.

The handle comprises a front cover, a window cover, a main body, and a back cover (Fig 6, top). The front cover provides an ergonomic grip. In order to balance the overall weight of the handle, the front cover and the back end were made of aluminum and Delrin, respectively, by CNC machining. The window cover was designed to fully allow LED light emission and protect the moving LEDs from being touched. The manipulator also incorporates a male Luer-Slip connector with a tool mount to accommodate conventional hypodermic needles. For other applications, the adaptor is replaceable with a variety of end-effectors such as a micro-pipette or laser probe.

The assembled instrument is 28.5 mm in diameter and 126 mm long, excluding the end-effector attached to the Luer-Slip adaptor. The total mass is 70.0 g, with the center of mass near the geometric center of the handle. Fig. 1 presents the fully assembled manipulator. The specifications of the 6-DOF Micron are summarized in Table I.

IV. CONTROL AND LINEARIZATION

The 6-DOF Micron is primarily controlled in link-length space using the inverse kinematics derived in the kinematics section; the goal position and current position of the tool tip are converted to six link-lengths by the inverse kinematics. Accordingly, we can define the error in each link in terms of length, which is subject to PID control. Fig. 7 presents the overall architecture of 6-DOF Micron, including a control
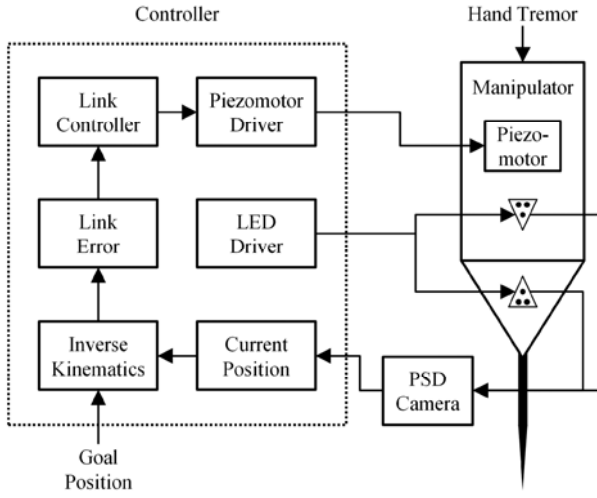
Fig. 7. Micron system architecture. For the feedback control of the manipulator, the goal position and current position are defined in terms of six link-lengths via inverse kinematics. Any undesired motion is regarded as a control disturbance, and the errors in the links are regulated by a PID controller.

Fig. 8. Linearization curve: velocity with respect to motor command (duty cycle).

scheme where the hand tremor is regarded as a control disturbance. Given the link errors, the motors are controlled by applying appropriate duty cycles to motor drivers (NSD-2101, New Scale Technologies, Inc., USA) that generate ultrasonic signals.

The SQUIGGLE motors are linearized before use in order to compensate the inconsistent performance that arises due to their inherent characteristics. Since the motor relies on the indirect driving method of orbital motion of the piezoelectric membrane on the nut, rather than directly rotating the threaded rod, the performance is sensitive to the external environment. The displacement and speed are dependent on supply voltage, applied frequency, and load. Operating temperature also affects the resonant frequency of the piezoelectric membrane. Furthermore, the bearing assembly has a large effect on the performance because the bearing itself restrains rotation somewhat, due to friction and mating tolerances. In addition, the side load provided by bending of the flexures may be significant. These effects may become pronounced in operation of such small actuators. Lastly, the applied preload on the motor yields asymmetric motion according to the direction of the motion. It is important to quantify the variation of the motors raised by these factors and manage the variation in control.

For the linearization process, the velocity of each motor is measured while applying the varying duty cycle of the command signal. As shown in Fig. 8, the response is nonlinear with respect to the motor command. To calibrate the motors, we constructed a table of motor command vs. velocity by making a fifth-degree polynomial fit to data recorded while the platform moved up and down along the z axis. The amplitude of the motion was modulated from 50 μm to 1.5 mm for 2.5 s. This process is also usable for monitoring degradation of the linear actuation module. In order to guarantee the performance of the motors, we constrain the slope of the curve at the zero command to be greater than 2 and the velocity values at ±0.8
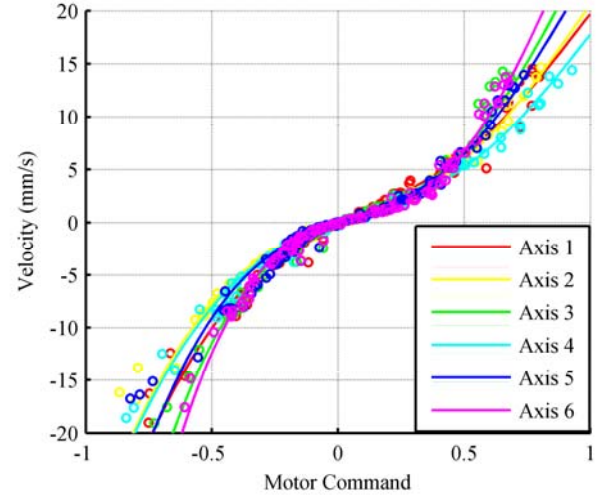
duty cycles to be greater than 10 mm/s. In case of a flat slope at the zero, there may be chattering on the motors when alternating the direction of motion. The lower values at the both ends of duty cycles limit the slew rate of the motors.

V. EXPERIMENTS AND RESULTS

A. Side Load Capability

We investigated the side load capability of the manipulator under varying side loads applied at an RCM which was 30 mm above the top of the tool mount. The range of the side loads was set from 0 to 0.3 N. A sinusoidal trajectory of ±1 mm amplitude was applied along the x-axis for duration of 4 s; the average speed over the total 4-mm stroke in each direction was 1 mm/s. The five trials were repeated for each side load.

Fig. 9 shows the resulting sinusoidal profiles corresponding to the different side loads. RMS error with respect to the goal
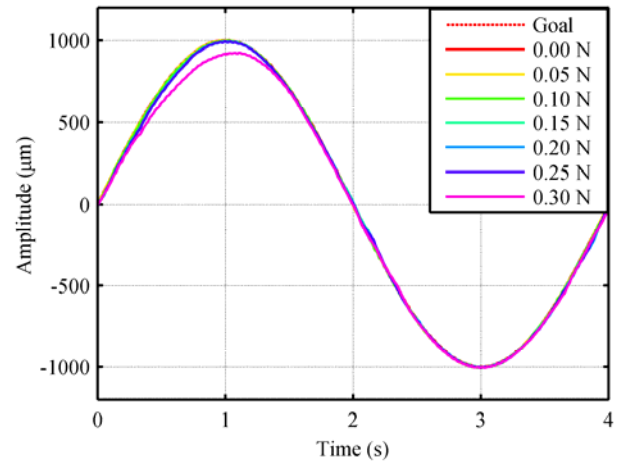
Fig. 9. Resulting trajectory with respect to the amount of the side load.

TABLE II
RMS ERRORS WITH RESPECT TO THE GOAL TRAJECTORIES FOR SIDE LOADS

Side Load (N)	0	0.05	0.1	0.15	0.20	0.25	0.30
Error (μm)	6	6	10	15	17	17	47

TABLE III
RMS ERRORS WITH RESPECT TO THE PLANNED TRAJECTORIES AND VARIOUS
VELOCITIES

Velocity (mm/s)	X (RCM)	X (Trans.)	Y (RCM)	Y (Trans.)	Z (Trans.)
1	8	7	6	7	11
2	8	7	7	9	22
5	16	9	14	13	43

The unit of the RMS error is μm.
RCM = Remote center of motion, Trans. = Transverse motion.

trajectory is summarized in Table II. Although the RMS error gradually increases until 0.25 N side load, the resulting profiles are still close to the sinusoidal goal trajectory. As the side load reaches 0.3 N, the distortion on the profile is markedly larger. These experimental results agree fairly well with the simulation done in the workspace analysis section assuming motor stall force of ±0.5 N.

B. Positioning Performance

Positioning performance was evaluated with respect to the five degrees of freedom that are important for the application. Axial rotation was excluded. Two angular motions were generated by pivoting about the RCM, parallel to the *x* and *y* axes, respectively. Three translations were also generated along *x*, *y*, and *z* axes by moving both the end-effector and the moving platform by the same amount of the amplitude. We adopted a sinusoidal profile as the reference trajectory with peak-to-peak amplitude of ±2 mm to cover the entire workspace. To investigate the positioning performance at different velocities up to the slew limit of the motor, the duration was varied from 1.6 to 8.0 s. Given the total travel, 8 mm, the average speed varied from 1 to 5 mm/s. The tests were also repeated for five trials and averaged. The RMS error with respect to the type of motion and the applied velocity is specified in Table III. Similar errors were observed for the angular and transverse motions along x and y axes, maintaining the error at less than 10 μm up to 2 mm/s velocity. In most cases, RMS error was doubled at 5 mm/s target velocity. RMS error was more prominent in transverse motion along the *z* axis than in other motions, even at lower velocities. This is primarily due to the relatively large radial play of the threaded rod in the SQUIGGLE® motor in order to generate orbital motion. It may cause transverse vibration while the moving platform is going up and down. The RMS error along the *z*-axis is only 14-25% of the total error, whereas the ratio in the Euclidean space would be 58 % (= $1/\sqrt{3}$) if error were equal in all three axes. In other words, most error in the *z*-axis translation was along the *x* and *y* axes. Furthermore, for the same amplitude of tip movement, a larger movement of the motors is needed for the *z*-axis translation than for the other motions. Since no angular motion is introduced along the end-effector, the amplitude of the end-effector is not amplified. This requires higher slew rates on the motors to make a longer stroke in the same amount of time.

C. Performance in Handheld Tasks

The manipulator was firmly affixed to a solid base in the previous experiments. Experiments in this section were conducted with the instrument held in the human hand, under a
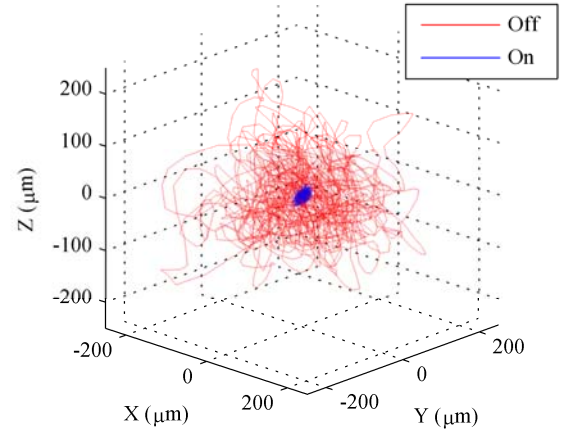

Fig. 10. Trajectory of the tool tip during a pointing task for 20 s. The red line indicates the trajectory without Micron assistance. The blue line is for the trajectory when Micron is activated.

board-approved protocol, by a single subject without surgical training.

1) Tremor cancellation

Tremor cancellation is the primary function of the handheld manipulator in microsurgery. In order to examine the canceling performance, a pointing task was introduced. A participant was asked to maintain a fixed tip position above a laser engraved rubber target for 20 s in each trial. All tasks were performed under a magnification of 25 x (Zeiss® OPMI™ surgical microscope). Once cancellation is activated, the current position of the tool tip is set as a goal position for control, and all disturbances from any source are rejected.

Fig. 10 illustrates one of the recorded trajectories for 20 s with and without cancellation. The RMS error and maximum error were calculated with respect to the 3D mean position of each trajectory for five trials. The RMS error drastically decreases from 112±8 μm to 12±2 μm on average by actively controlling the tool tip; the difference is statically significant ($p = 3\times10^{-9}$). The maximum error is an important measure of hand tremor reduction since even a single large excursion may cause collateral damage in microsurgery. The mean maximum error is 361 and 49 μm for the "off" and "on" cases, respectively. The difference in maximum error is also statistically significant ($p = 7\times10^{-6}$).

2) Circle tracing

In order to evaluate positioning performance during handheld operation, various sizes of circle patterns were introduced from 1 to 4 mm in diameter. Such patterns can be useful for laser retinal photocoagulation as treatment for macular degeneration in the eye [18], and for semiautomated scanning for retinal optical coherence tomography [38]. The range of velocities was varied from 1 to 5 m/s to find the most efficient velocity while maintaining desired accuracy with high speed. The automated circle-tracing was also compared to manual tracing without the aid of Micron. In the manual trials, the subject traced circles as well as possible above a printed target, without velocity regulation. Fig. 11(a) shows the RMS error corresponding to the varying velocities and the sizes of the circles in diameter. Overall average error for five trials
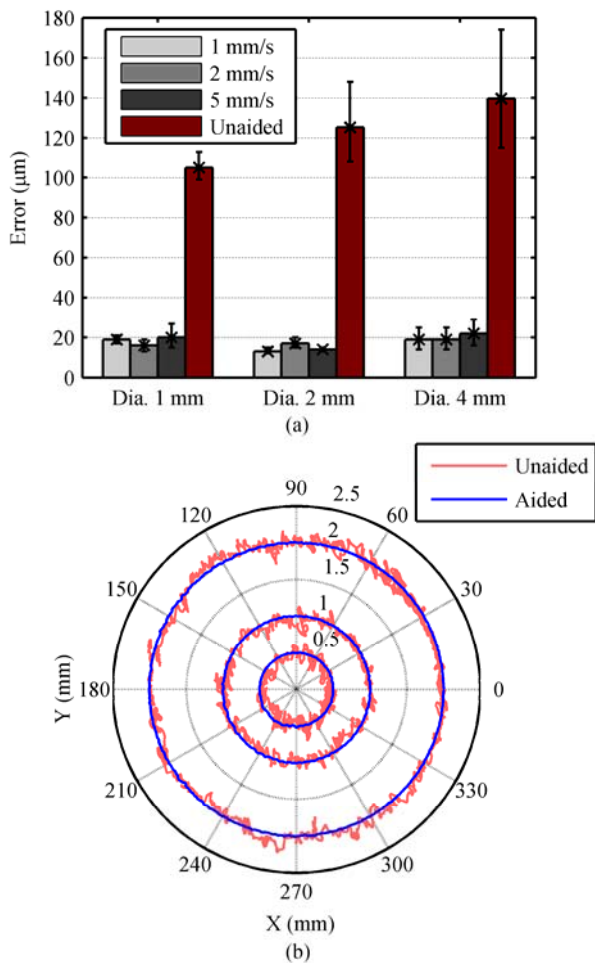
Fig. 11. (a) RMS error during automatic handheld circle-tracing with various circle diameters and tracking velocities. (b) Trajectory of circle-tracing for various sizes of circles.

ranges from 10 to 20 μm for the automated circle-tracing. The error exceeds 20 μm under the circle tracing of 4 mm diameter with a velocity of 5 mm/s. Nevertheless, the resulting trajectory, with a velocity of 5 mm/s (shown in Fig. 11(b)), is still acceptable in laser surgery, given the relatively large size of a laser spot (200-300 μm). RMS errors in circle-tracing at 1- and 2-mm diameter are less than the error at 4-mm diameter since the manipulator operates near the edge of the workspace with large angular motion. Interestingly, the error in circle tracing of 2-mm diameter is somewhat less than the error at 1-mm diameter, possibly due to the fact that circle tracing in the smaller circle is affected by the comparable amplitude of hand tremor; i.e., the signal-to-noise ratio is lower. Compared to the automated trials, the errors in the manual tracing are significantly larger and gradually increase with the sizes of the circles, from 105 to 140 μm. The average velocities range from 0.3–0.4 mm/s, increasing slightly with circle diameter; this is an order of magnitude slower than the automated tracing.

VI. Discussion

We demonstrated the design and performance of the handheld tremor-canceling manipulator. In order to realize the miniature 6-DOF manipulator, the design was optimized, focusing primarily on the amount of tolerable side load

introduced at an RCM during vitreoretinal surgery. This is of particular importance for this system due to a trade-off between the tolerable side load and the size of the manipulator (particularly the diameter), given the limited force capability of the miniature actuators used. The mechanical design and control have been refined to improve the performance of the linear actuation module by taking into account the underlying characteristics of the SQUIGGLE® motor. In addition, an ergonomic handle was combined with the manipulator, enclosing also the ASAP system and embedded electronics for handheld operation. The fully handheld manipulator successfully tolerates side load up to 0.25 N without significant degradation. In particular, in a pointing task, the manipulator shows about 89.3% tremor reduction compared to unaided trials. The performance of the 6-DOF Micron is difficult to compare directly to results from other tremor-canceling devices due to the variation in hand tremor with differences in task kinematics, task ergonomics, and execution time. Nonetheless, the error-reduction ratio can be compared under similar settings. The pointing task in the 6-DOF Micron is comparable to the task done in the 3-DOF Micron with a virtual fixture which applies a constant goal position to the tool tip [39]. The result with a hard-virtual fixture control shows similar performance in tremor-reduction: 81.8% reduction in maximum error compared to unaided trials. The result is also comparable to the error reduction achieved recently by a teleoperated surgical robot operated by surgeons (from 90.0 μm to 14.9 μm; an 83.6% reduction) [40]. The benefit of the large range of motion in the new 6-DOF Micron was explored in fully automatic circle-tracing; the error obtained is smaller than is attainable in freehand operation [18]. The goal of these tests is to quantify the best the system is capable of, under idealized conditions, as a baseline for comparison with future performance under more realistic conditions.

In comparison to the 3-DOF piezo-bender manipulator [15], the new 6-DOF Micron offers six degrees of freedom and an order-of-magnitude larger range of motion with adequate force capability and slew rate. It enables real-world use of the handheld manipulator, since it is capable of imposing an RCM during surgery, and also avoiding the saturation in actuation which frequently occurred in the 3-DOF Micron, hindering effective compensation. To be used in real surgery, the manipulator should be able to preserve the surgeon's voluntary motion while rejecting hand tremor. Hence, we have adopted control algorithms such as lowpass/shelving filtering schemes developed in the 3-DOF Micron for this type of handheld operation [15]. However, the practical consequence is that the canceling performance is currently limited by a chattering instability in the range of 50-100 Hz. We expect to be able to mitigate the instability by analyzing and managing the performance of actuation modules on an individual basis. In addition, nonlinear control algorithms may help minimize the adverse effects of stick-slip nonlinearities.

Further experiments will also be performed on various tasks *ex vivo* and *in vivo* with multiple subjects in order to rigorously confirm the handheld performance improvement. Moreover, the automatic scanning functionality will be utilized in laser

photocoagulation, combined with CCD cameras and stereo-vision algorithms to specify a desired trajectory in the 3D ASAP coordinates for control, as in [39]. For such an automated operation, tracking features should also be implemented to compensate for any eye movement induced by voluntary motion and/or tremor [41], [42].

REFERENCES

[1] G. Dogangil, B. L. Davies, and F. Rodriguez y Baena, "A review of medical robotics for minimally invasive soft tissue surgery," *Proc. Inst. Mech. Eng. H.*, vol. 224, no. 5, pp. 653–679, May 2010.

[2] S. Najarian, M. Fallahnezhad, and E. Afshari, "Advances in medical robotic systems with specific applications in surgery-a review," *J. Med. Eng. Technol.*, vol. 35, no. 1, pp. 19–33, Jan. 2011.

[3] Y. Sun and B. J. Nelson, "Biological cell injection using an autonomous microrobotic system," *Int. J. Robot. Res.*, vol. 21, no. 10–11, pp. 861–868, Oct. 2002.

[4] S. M. Prasad, S. M. Prasad, H. S. Maniar, C. Chu, R. B. Schuessler, R. J. Damiano, and R. J. Damiano Jr, "Surgical robotics: impact of motion scaling on task performance," *J. Am. Coll. Surg.*, vol. 199, no. 6, pp. 863–868, Dec. 2004.

[5] A. R. Lanfranco, A. E. Castellanos, J. P. Desai, and W. C. Meyers, "Robotic surgery: a current perspective," *Ann. Surg.*, vol. 239, no. 1, pp. 14–21, Jan. 2004.

[6] H. B. Huang, S. Dong, J. K. Mills, and C. Shuk Han, "Robotic cell injection system with position and force control: toward automatic batch biomanipulation," *IEEE Trans. Robot.*, vol. 25, no. 3, pp. 727–737, 2009.

[7] I. W. Hunter, T. Doukoglou, S. R. Lafontaine, P. G. Charette, L. A. Jones, M. A. Sagar, G. D. Mallinson, and P. J. Hunter, "A teleoperated microsurgical robot and associated virtual environment for eye surgery," *Presence*, vol. 2, no. 4, pp. 265–280, 1993.

[8] P. S. Schenker, H. Das, and T. R. Ohm, "A new robot for high dexterity microsurgery," in *Conf. Comput. Vis. Virtual Real. Robot. Med.*, 1995, vol. 905, pp. 115–122.

[9] D. H. Bourla, J. P. Hubschman, M. Culjat, A. Tsirbas, A. Gupta, and S. D. Schwartz, "Feasibility study of intraocular robotic surgery with the da Vinci Surgical System," *Retina*, vol. 28, no. 1, pp. 154–158, 2008.

[10] M. Shoham, M. Burman, E. Zehavi, L. Joskowicz, E. Batkilin, and Y. Kunicher, "Bone-mounted miniature robot for surgical procedures: concept and clinical applications," *IEEE Trans. Robot. Autom.*, vol. 19, no. 5, pp. 893–901, Oct. 2003.

[11] M. L. Nordlund, D. M. V Marques, F. F. Marques, R. J. Cionni, and R. H. Osher, "Techniques for managing common complications of cataract surgery.," *Curr. Opin. Ophthalmol.*, vol. 14, no. 1, pp. 7–19, 2003.

[12] R. Taylor, P. Jensen, L. Whitcomb, A. Barnes, R. Kumar, Stoianovici, D. Gupta, Wang, E. De Juan, and L. Kavoussi, "A steady-hand robotic system for microsurgical augmentation," *Int. J. Robot. Res.*, vol. 18, no. 12, pp. 1201–1210, Dec. 1999.

[13] B. Mitchell, J. Koo, M. Iordachita, P. Kazanzides, A. Kapoor, J. Handa, G. Hager, and R. Taylor, "Development and application of a new Steady-Hand manipulator for retinal surgery," in *Proc. IEEE Int. Conf. Robot. Autom.*, 2007, pp. 623–629.

[14] S. Yang, R. A. MacLachlan, and C. N. Riviere, "Design and analysis of 6 DOF handheld micromanipulator," in *Proc. IEEE Int. Conf. Robot. Autom.*, 2012, pp. 1946–1951.

[15] R. A. Maclachlan, B. C. Becker, J. C. Tabarés, G. W. Podnar, L. A. Lobes, and C. N. Riviere, "Micron : an actively stabilized handheld tool for microsurgery," *IEEE Trans. Robot.*, vol. 28, no. 1, pp. 195–212, 2012.

[16] R. H. Taylor and D. Stoianovici, "Medical robotics in computer-integrated surgery," *IEEE Trans. Robot. Autom.*, vol. 19, no. 5, pp. 765–781, 2003.

[17] P. S. Jensen, K. W. Grace, R. Attariwala, J. E. Colgate, and M. R. Glucksberg, "Toward robot-assisted vascular microsurgery in the retina," *Graefes Arch. Clin. Exp. Ophthalmol.*, vol. 235, no. 11, pp. 696–701, 1997.

[18] B. C. Becker, R. A. MacLachlan, L. A. Lobes, and C. N. Riviere, "Semiautomated intraocular laser surgery using handheld instruments.," *Lasers Surg. Med.*, vol. 42, no. 3, pp. 264–273, 2010.

[19] A. Ramadan, K. Inoue, T. Arai, and T. Takubo, "New architecture of a hybrid two-fingered micro-nano manipulator hand: optimization and design," *Adv. Robot.*, vol. 22, no. 2–3, pp. 235–260, 2008.

[20] J. Peirs, D. Reynaerts, and H. Van Brussel, "Design of miniature parallel manipulators for integration in a self-propelling endoscope," *Sens. Actuators. A. Phys.*, vol. 85, no. 1–3, pp. 409–417, 2000.

[21] U.-X. Tan, W. T. Latt, C. Y. Shee, and W. T. Ang, "A low-cost flexure-based handheld mechanism for micromanipulation," *IEEE/ASME Trans. Mechatronics*, vol. 16, no. 4, pp. 773–778, Aug. 2011.

[22] D. Choi and C. Riviere, "Flexure-based manipulator for active handheld microsurgical instrument," in *Proc. 27th Annu. Int. Conf. IEEE Eng. Med. Biol. Soc.*, 2005, pp. 2325–2328.

[23] S. Yang, R. A. MacLachlan, and C. N. Riviere, "Performance of a six-axis handheld microsurgical robot with ultrasonic linear motors," in *ASME 5th Annu. Dyn. Syst. Control Conf.*, 2012, pp. 395–402.

[24] V. E. Gough, "Contribution to discussion of papers on research in automobile stability, control and tyre performance," *Proc. Auto. Div. Inst. Mech. Eng.*, vol. 171, pp. 392–394, 1956.

[25] D. Stewart, "A platform with six degrees of freedom," *Proc. Inst. Mech. Eng*, vol. 180, no. 1, pp. 371–386, 1965.

[26] M. S. Fee and A. Leonardo, "Miniature motorized microdrive and commutator system for chronic neural recording in small animals," *J. Neurosci. Meth.*, vol. 112, no. 2, pp. 83–94, 2001.

[27] S. Yang, J. Cho, S. Lee, K. Park, J. Kim, Y. Huh, E.-S. Yoon, and H.-S. Shin, "Feedback controlled piezo-motor microdrive for accurate electrode positioning in chronic single unit recording in behaving mice," *J. Neurosci. Meth.*, vol. 195, no. 2, pp. 117–127, 2011.

[28] N. M. Thanh, V. Glazunov, and L. N. Vinh, "Determination of constraint wrenches and design of parallel mechanisms," in *Int. Conf. Elect. Eng. Comput. Sci. Autom. Control*, 2010, pp. 46–53.

[29] I. A. Bonev, D. Zlatanov, and C. M. Gosselin, "Singularity analysis of 3-DOF planar parallel mechanisms via screw theory," *J. Mech. Des.*, vol. 125, no. 3, pp. 573–581, 2003.

[30] X.-J. Liu, J. Wang, F. Gao, and L.-P. Wang, "On the design of 6-DOF parallel micro-motion manipulators," in *Proc. IEEE/RSJ Int. Conf. Intell. Robot. Syst.*, 2001, vol. 1, pp. 343–348.

[31] K.-K. Oh, X.-J. Liu, D. S. Kang, and J. Kim, "Optimal design of a micro parallel positioning platform. Part I: Kinematic analysis," *Robotica*, vol. 22, no. 6, pp. 599–609, Nov. 2004.

[32] A. D. Jagtap and C. N. Riviere, "Applied force during vitreoretinal microsurgery with handheld instruments," in *Proc. 26th Annu. Int. Conf. IEEE Eng. Med. Biol. Soc.*, 2004, vol. 4, pp. 2771–2773.

[33] C. Gosselin and J. Angeles, "Singularity analysis of closed-loop kinematic chains," *IEEE Trans. Robot. Autom.*, vol. 6, no. 3, pp. 281–290, 1990.

[34] R. A. MacLachlan and C. N. Riviere, "High-speed microscale optical tracking using digital frequency-domain multiplexing," *IEEE Trans. Instrum. Meas.*, vol. 58, no. 6, pp. 1991–2001, Jun. 2009.

[35] C. N. Riviere, W. T. Ang, and P. K. Khosla, "Toward active tremor canceling in handheld microsurgical instruments," *IEEE Trans. Robot. Autom.*, vol. 19, no. 5, pp. 793–800, 2003.

[36] W. T. Ang, P. K. Khosla, and C. N. Riviere, "Kalman filtering for real-time orientation tracking of handheld microsurgical instrument," in *Proc. IEEE/RSJ Int. Conf. Intell. Robot. Syst.*, 2004, vol. 3, pp. 2574–2580.

[37] W. T. Latt, U.-X. Tan, C. Y. Shee, C. N. Riviere, and W. T. Ang, "Compact sensing design of a handheld active tremor compensation instrument," *IEEE Sens. J.*, vol. 9, no. 12, pp. 1864–1871, 2009.

[38] S. Yang, M. Balicki, R. A. MacLachlan, X. Liu, J. U. Kang, R. H. Taylor, and C. N. Riviere, "Optical coherence tomography scanning with a handheld vitreoretinal micromanipulator," in *Proc. 34th Annu. Int. Conf. IEEE Eng. Med. Biol. Soc.*, 2012, pp. 948–951.

[39] B. C. Becker, R. A. MacLachlan, L. A. Lobes, G. D. Hager, and C. N. Riviere, "Vision-based control of a handheld surgical micromanipulator with virtual fixtures," *IEEE Trans. Robot.*, vol. 29, no. 3, pp. 674–683, Jun. 2013.

[40] Y. Noda, Y. Ida, S. Tanaka, T. Toyama, M. F. Roggia, Y. Tamaki, N. Sugita, M. Mitsuishi, and T. Ueta, "Impact of robotic assistance on precision of vitreoretinal surgical procedures," *PLoS One*, vol. 8, no. 1, p. e54116, 2013.

[41] B. C. Becker and C. N. Riviere, "Real-time retinal vessel mapping and localization for intraocular surgery," in *Proc. IEEE Int. Conf. Robot. Autom.*, 2013, pp. 5360–5365.

[42] M. R. Burkhardt, T. D. Soper, W. J. Yoon, and E. J. Seibel, "Controlling the trajectory of a flexible ultrathin endoscope for fully automated bladder surveillance," *IEEE /ASME Trans. Mechatronics*, vol. 19, no. 1, pp. 366–373, 2014.